Long-Lived Isospin Excitations in Magic-Angle Twisted Bilayer Graphene

Authors: Tian Xie[1], Siyuan Xu[1], Zhiyu Dong[2], Zhiyuan Cui[1], Yunbo Ou[3], Melike Erdi[3], Kenji Watanabe[4], Takashi Taniguchi[5], Seth A. Tongay[3], Leonid S. Levitov[6], Chenhao Jin[1]*

Affiliations:

[1]Department of Physics, University of California at Santa Barbara, Santa Barbara, CA, USA

[2]Department of Physics and Institute for Quantum Information and Matter, California Institute of Technology, Pasadena, CA, USA

[3]Materials Science and Engineering, School for Engineering of Matter, Transport and Energy, Arizona State University, Tempe, AZ, USA

[4]Research Center for Electronic and Optical Materials, National Institute for Materials Science, 1-1 Namiki, Tsukuba, Japan

[5]Research Center for Materials Nanoarchitectonics, National Institute for Materials Science, 1-1 Namiki, Tsukuba, Japan

[6]Department of Physics, Massachusetts Institute of Technology, Cambridge, MA, USA

* Corresponding author. Email: jinchenhao@ucsb.edu

A plethora of correlated many-body phases, both conventional and exotic, have been reported in magic-angle twisted bilayer graphene (MATBG)[1-24]. However, the dynamics associated with these correlated states, crucial for understanding the underlying physics, remains unexplored. Here we combine exciton sensing and optical pump-probe spectroscopy to investigate dynamics of isospin orders in MATBG with WSe_2 substrate across the entire flatband, achieving sub-picosecond resolution. We observe remarkably slow isospin dynamics in a broad filling range around $\nu = 2$ and between $\nu = -3$ and -2, with lifetimes up to 300ps that decouple from the much faster cooling of electronic temperature (~10ps). This non-thermal behavior demonstrates the presence of abnormally long-lived modes in the isospin degrees of freedom. This surprising observation, not anticipated by theory, implies the existence of long-range propagating collective modes, strong isospin fluctuations and memory effects; and is likely associated with an intervalley coherent (IVC) or incommensurate Kekulé spiral (IKS) ground state. We further demonstrate non-equilibrium control of the isospin orders previously found around integer fillings. Specifically, through ultrafast manipulation, it can be transiently shifted away from integer fillings. Our study demonstrates a unique probe of collective excitations in MATBG and paves the way for actively controlling non-equilibrium phenomena in moiré systems.

Magic-angle twisted bilayer graphene (MATBG) recently emerged as an intriguing platform for engineering correlated phenomena[1–24]. The electron isospin degrees of freedom – spin and valley – play a critical role in its phase diagram with superconductivity often emerging adjacent to isospin transitions[3–8]. The rich variety of isospin orders offers a unique opportunity to explore the interplay between electron correlation and topology[9–14]. At low temperatures, symmetry-broken isospin phases are reported in MATBG at integer fillings of the moiré unit cell. Their exact nature is under active investigation, with the candidate orders including multiple types of spin/valley polarized states and IVC states[25–28]. At higher temperature of T >5K, the long-range isospin orders are expected to melt. Cascade features near integer fillings were found to persist up to tens of Kelvin in compressibility and chemical potential measurements. This puzzling behavior was generally interpreted as a signature of parent correlated states of the low temperature isospin orders arising due to short-range isospin correlations[19–22].

One intriguing question posed by these findings is about the impact of isospin orders on system dynamics. It has been conjectured that the isospin soft modes can provide the pairing glue for superconductivity[29–34] and contribute to the large electronic entropy in transport at elevated temperature[22–24]. However, the isospin orders typically feature exotic order parameters that are difficult to couple to, making susceptibility measurements challenging. Non-equilibrium dynamics offers a promising alternative route to probe this physics. By inspecting the transient dynamics between isospin orders and the damping of collective excitations, one could access the flatness of the energy landscape and key properties of the soft isospin modes without directly coupling to the order parameter[33–37]. However, isospin dynamics of flatband graphene systems has remained unexplored in experiment due to the lack of suitable ultrafast probes. Available techniques such as time-resolved photovoltage are only sensitive to electronic temperature but not the isospin degrees of freedom[38].

Non-equilibrium dynamics of isospin orders

Here we develop a novel optical pump probe technique to directly access ultrafast dynamics of isospin orders in MATBG and inspect damping of collective isospin excitations. Fig. 1a illustrates the experimental scheme, where a monolayer WSe_2 sensor is placed adjacent to the MATBG without an hBN spacer. The interaction between electrons in graphene and WSe_2 excitons converts low-energy isospin orders in graphene into exciton responses at optical frequency. Fig. 1b shows the gate-dependent equilibrium reflection contrast (RC) spectrum of device D1 (~1.04° twisted) at the base temperature of 2.5K (see methods). Since the Dirac points of graphene are positioned deep inside the bandgap of WSe_2, all gate-injected charges reside in graphene while WSe_2 remains charge neutral. Therefore, the WSe_2 1s exciton (blue arrows) remains largely intact as the overall doping increases except for a slight redshift. In contrast, the WSe_2 2s exciton (yellow arrows) shows rich features due to its sensitivity to the dielectric environment and MATBG's polarizability[39,40]. It can thus distinguish different isospin polarized states due to their different Fermiology (see methods). A series of cascade features emerge around integer fillings between ν = -4 and 4, which are reminiscent of chemical potential measurements and are assigned to the parent states of symmetry-broken isospin orders[14–16].

The observed cascade features indicate our measurement's sensitivity to the isospin degree of freedom, which allows us to further investigate its non-equilibrium dynamics through pump probe spectroscopy. Fig. 1c shows the non-equilibrium RC of device D1 at representative pump-probe delays Δt = -3.7, 1, 10 and 136 ps, respectively (see methods). See Supplementary Movie 1 and 2 for complete time evolution. We use pump photon energy of 1.55eV to selectively excite graphene but not WSe_2. All the pump-induced changes in RC therefore originate from excitations in graphene while WSe_2 itself remains in equilibrium, as confirmed by the lack of change in 1s exciton response (Fig. 1c lower panels and Fig. 1d). We have further performed systematic measurements of pump wavelength dependence and probe fluence dependence to demonstrate that the WSe_2 layer remains as a passive sensor (see methods).

To investigate the non-equilibrium dynamics of isospin orders, we measure the filling-dependent relaxation in device D1 (see methods). Fig. 2a shows the time evolution of the pump-induced RC change, ΔRC, at representative fillings near $\nu = 2$ (see Supplementary Movie 3 for full filling dependence). Each panel corresponds to a fixed filling factor. The ΔRC signal remains zero before the pump arrives and rises sharply at time zero; then gradually diminishes as the system relaxes back to equilibrium. At fillings away from $\nu = 2$, such decay is rather fast and the signal merges into the noise floor after ~40ps. Surprisingly, a prominent slowing-down of the dynamics is observed near $\nu = 2$, where the signal develops a long tail that barely changes over the full delay range of 130ps. Similar slowing-down is also observed on the hole side between $\nu = -3$ and -2. (Fig. 2b), where, interestingly, it peaks notably at away from integer filling. Fig. 2c summarizes the filling-dependent ΔRC signal between $\nu = -5$ and 5 at probe energy of the 2s exciton resonance, and the fitted relaxation lifetime is shown in Fig. 2d (blue curve). The single exponential fitting used here considerably underestimates the lifetime of the long relaxation components and only provides qualitative information (see methods). Nevertheless, we already see a clear slowing-down of relaxation around $\nu = 2$, -2.3 and ±4. In contrast, no apparent slowing down is observed around $\nu = \pm 1$ or ±3. These behaviors are well reproduced in two other MATBG devices D2 and D3 (see Extended Data Fig. 1 and 7).

The enhanced lifetime at $\nu = \pm 4$ is consistent with previous photovoltage measurements of electronic temperature[38], which is assigned to a gap-induced phonon bottleneck that prevents efficient cooling. On the other hand, the slowing-down around $\nu = 2$ and -2.3 is quite surprising as it does not show up in the electronic temperature measurement. In fact, the cooling was found to be accelerated over the entire filling range of $-4<\nu<4$ with a near-constant lifetime of 5ps[38]. To elucidate origin of the slowing-down around $\nu = 2$ and -2.3, we perform measurements on a non-magic-angle device D3 that does not have apparent cascade features in the equilibrium RC (~1.14° twist, see Extended Data Fig. 2 and Supplementary Movie 4). While we find similarly enhanced lifetime at $\nu = \pm 4$, the slowing-down elsewhere is much weaker (Fig. 2d, orange curve). We have further measured the temperature dependence. Fig. 3a summarizes the relaxation dynamics in device D1 at equilibrium temperature from 2.5 to 10K. The slowing-down around $\nu = 2$ and -2.3 shows sensitive temperature dependence and largely disappears at 10K (Fig. 3b). In contrast, the lifetime at $\nu = \pm 4$ remains intact. These measurements indicate the distinctively different origins behind the slow relaxation around $\nu = 2$ and -2.3 and at ±4. While the latter is consistent with a single-particle picture, the former necessarily originates from correlation effects.

Decoupling between the charge and isospin dynamics

Electron correlations can alter the relaxation dynamics in multiple ways. The simplest scenario is a phonon bottleneck induced by a correlated gap, which slows down the cooling of electronic temperature. This scenario is conceptually similar to $\nu = \pm 4$ since in both cases the dynamics corresponds to the charge degree of freedom. On the other hand, it is also possible that the slowing-down is driven by the isospin degree of freedom, such as from a slow transition between isospin orders. To elucidate the mechanism, Fig. 3c shows the time-dependent ΔRC at $\nu = 2.07$ over a larger delay range of 300ps. The signal remains visible in the full delay range. In contrast, the signal around $\nu = 4$, despite its larger initial amplitude, becomes negligible at 300ps (Fig. 3d). Fig. 3e summarizes the relaxation dynamics around $\nu = 2$ and 4 (symbols). To reliably extract the lifetime of the slow component, we fit the experimental data after 50ps with single exponential decay (dashed lines). The lifetime at $\nu = 2.07$ approaches 300ps, much longer than the lifetime of 60ps at $\nu = 3.95$. Such dramatic slowing-down around $\nu = 2$ cannot be accounted for by a gap-induced phonon bottleneck since the gap at $\nu = 2$, if exists, is much smaller than the gap at $\nu = 4$. Indeed, previous photovoltage measurement reported negligible slowing-down of electronic cooling at $\nu = 2$ despite insulating transport[3–5,38]. Furthermore, the maximum slowing-down on the hole side corresponds to a gapless metallic state away from integer filling (Fig. 3f) and is qualitatively incompatible with the electronic temperature cooling scenario[38]. These observations indicate that the slow dynamics around $\nu = 2$ and -2.3 does not originate from the charge degree of freedom.

A close inspection of the relaxation process further allows us to extract the charge and isospin dynamics separately. The complete melting of cascade features at time zero indicates a high initial electronic temperature of >100K (Fig. 1c). Meanwhile, since the slow component in relaxation only exists at low temperature, the dominance of the slow component at $\Delta t = 30$ps (Fig. 3e) indicates that the system temperature is already below 10K at this point. Such rapid decrease of electronic temperature gives a carrier cooling lifetime of <10ps around $\nu = 2$, consistent with previous reports[38]. The ~300ps relaxation time is therefore completely decoupled from the charge dynamics and should originate from the isospin degree of freedom. Indeed, the dynamics around $\nu = 2$ or -2.3 is described by a two-component decay corresponding to the charge and isospin dynamics, respectively (Fig. 3 e-f, red lines), while the dynamics at $\nu = \pm 4$ shows a single-exponential decay from the electronic cooling (blue lines). Consequently, only the $\nu = \pm 4$ feature is observed in photovoltage measurements that probe the electronic temperature[38]. On the other hand, the sensitivity of our measurements to isospin orders (Fig. 1b) allows us to capture dynamics in both the charge and isospin degrees of freedom. Their complete decoupling around $\nu = 2$ and -2.3 is further confirmed by the pump fluence dependence (see methods and Extended Data Fig. 3).

Control of the cascade isospin-order features

Besides direct access to the isospin dynamics, our experimental scheme also enables ultrafast engineering of non-equilibrium states in MATBG. To this end, we focus on the responses of MATBG at short timescales of ≤20 ps. A careful inspection of the transient RC at $\Delta t = 10$ps (Fig. 1c) reveals shifts of the cascade features to higher fillings compared to their equilibrium positions (arrows). To investigate the shifts in detail, we extract the filling-dependent 2s exciton energy at each delay and monitor its evolution over time, as shown in Fig. 4a (see methods). Before time zero, the 2s exciton energy shows local maxima at integer fillings, corresponding to the cascade features. Upon the pump arrival, all cascade features are quenched in amplitude, as expected from a sudden increase of electronic temperature. On the other hand, their positions also transiently shift. Fig. 4b summarizes the time-dependent positions of the cascade features. The cascade features at $\nu = 2, 3$ and 4 shifts to higher fillings within ~2ps of pump excitation and recovers over a timescale of 5, 10 and 40ps, respectively. These behaviors are well-reproduced in another MATBG device D2 (see Supplementary Movie 5). Such prominent shifts of cascade features are not compatible with a simple equilibrium temperature change, which only reduces their amplitude but does not change their fillings (see Extended Data Fig. 4). Therefore, they are necessarily non-equilibrium phenomena at ultrafast timescale.

Discussions and conclusions

We first discuss the origin of the ultrafast shifts (see methods for more discussions). They can naturally arise from a bottleneck in carrier relaxation between the remote- and flat-bands (Fig. 4c). At $\nu = 4$, such a bottleneck is confirmed by our observation of an enhanced electronic cooling time of ~60ps (Fig. 3e), which is comparable to the recovery time of the transient shift (Fig. 4b) and supports a common origin. The transient shifts at $\nu = 2$ and 3 probably originate from similar mechanisms. This picture allows us to determine the filling-dependent carrier relaxation dynamics between the remote bands and flat-bands in MATBG and indicates a prominent electron-hole asymmetry: the hole relaxation is always efficient (<2ps) in electron-doped MATBG; whereas the electron relaxation is rather slow around $\nu = 4$ (40ps) and becomes faster at lower fillings, reaching 10ps around $\nu = 3$ and 5ps around $\nu = 2$. Such relaxation time is consistent with the charge dynamics determined in Fig. 3 (<10ps at $\nu = 2$). The shift around $\nu = 1$ is not noticeable, which could be due to an even faster electron relaxation and/or restored electron-hole symmetry.

We now discuss the abrupt slowing-down of isospin dynamics around $\nu = 2$ and between $\nu = -3$ and -2, which is orders-of-magnitude slower than the carrier relaxation and is clearly more exotic. Magnetic orders in the valley and spin degrees of freedom would naturally lead to isospin collective modes associated with long-wavelength dynamics of the isospin order parameter. Such modes, when excited under optical excitation, will relax at characteristic times originating from collective dynamics. This would yield lifetimes that are considerably longer than those of single-particle processes at fillings $\nu = 0$ and ± 4 (see methods). This picture naturally accounts for long-lived isospin excitations at integer moiré fillings such as at $\nu = 2$, where the insulating ground state leads to a gap in the particle-hole continuum. Such gap suppresses damping of the collective isospin waves as long as the isospin modes are softer than the gap size (see methods).

In addition, intriguingly, we also consistently observe dramatic slowing-down of isospin dynamics away from integer fillings at $-3<\nu<-2$ (Fig. 2, Extended Data Fig. 1 and 7). In-situ transport (Extended Data Fig. 7) further confirms that the slowest isospin dynamics on the hole-doped side appears within a gapless metallic phase. This suggests the presence of a gapless collective mode that only couples to the isospin degree of freedom. To host a mode of this type, the ground state is likely to be an IVC or IKS state[26] where broken U(1) symmetry leads to a gapless Goldstone mode (see methods). Indeed, IKS states have recently been observed in a similar filling range of $-3<\nu<-2$ through STM measurements (Ref. [26–28]), supporting our interpretation.

Our study also has interesting implications for the collective isospin dynamics. Although IKS states detected in STM measurements[28] can host gapless isospin modes, it was unclear whether these isospin modes are long-lived or strongly damped. Long-lived isospin modes are expected to show long-range propagation and strong fluctuations, where strongly damped modes would not show this behavior. Our results indicate that the isospin soft modes are weakly-damped at $-3<\nu<-2$. Interestingly, superconductivity in MATBG is also most widely observed at $-3<\nu<-2$ (Ref. [3–5]), and strong isospin fluctuations have been conjectured as a potential pairing glue for superconductivity[30–34]. Additionally, transport measurements[21] indicate signatures of isospin fluctuations at elevated temperatures, which is consistent with the long-lived excitations observed in our measurements above the ordering temperature. By probing these effects, our work offers a crucial missing piece in understanding correlated physics in flatband graphene systems.

Main Text References

1. Utama, M. I. B. *et al.* Visualization of the flat electronic band in twisted bilayer graphene near the magic angle twist. *Nat Phys* **17**, 184–188 (2021).

2. Yoo, H. *et al.* Atomic and electronic reconstruction at the van der Waals interface in twisted bilayer graphene. *Nat Mater* **18**, 448–453 (2019).

3. Yankowitz, M. *et al.* Tuning superconductivity in twisted bilayer graphene. *Science (1979)* **363**, 1059–1064 (2019).

4. Cao, Y. *et al.* Unconventional superconductivity in magic-angle graphene superlattices. *Nature* **556**, 43–50 (2018).

5. Saito, Y., Ge, J., Watanabe, K., Taniguchi, T. & Young, A. F. Independent superconductors and correlated insulators in twisted bilayer graphene. *Nat Phys* **16**, 926–930 (2020).

6. Kim, H. *et al.* Evidence for unconventional superconductivity in twisted trilayer graphene. *Nature* **606**, 494–500 (2022).

7. Lu, X. *et al.* Superconductors, orbital magnets and correlated states in magic-angle bilayer graphene. *Nature* **574**, 653–657 (2019).

8. Arora, H. S. *et al.* Superconductivity in metallic twisted bilayer graphene stabilized by WSe2. *Nature* **583**, 379–384 (2020).

9. Xie, Y. *et al.* Fractional Chern insulators in magic-angle twisted bilayer graphene. *Nature* **600**, 439–443 (2021).

10. Das, I. *et al.* Symmetry-broken Chern insulators and Rashba-like Landau-level crossings in magic-angle bilayer graphene. *Nat Phys* **17**, 710–714 (2021).

11. Bultinck, N., Chatterjee, S. & Zaletel, M. P. Mechanism for Anomalous Hall Ferromagnetism in Twisted Bilayer Graphene. *Phys Rev Lett* **124**, (2020).

12. Khalaf, E., Chatterjee, S., Bultinck, N., Zaletel, M. P. & Vishwanath, A. Charged skyrmions and topological origin of superconductivity in magic-angle graphene. *Sci Adv* **7**, (2021).

13. Grover, S. *et al.* Chern mosaic and Berry-curvature magnetism in magic-angle graphene. *Nat Phys* **18**, 885–892 (2022).

14. Yu, J. *et al.* Spin skyrmion gaps as signatures of strong-coupling insulators in magic-angle twisted bilayer graphene. *Nat Commun* **14**, 6679 (2023).

15. Cao, Y. *et al.* Correlated insulator behaviour at half-filling in magic-angle graphene superlattices. *Nature* **556**, 80–84 (2018).

16. Wong, D. *et al.* Cascade of electronic transitions in magic-angle twisted bilayer graphene. *Nature* **582**, 198–202 (2020).

17. Wu, S., Zhang, Z., Watanabe, K., Taniguchi, T. & Andrei, E. Y. Chern insulators, van Hove singularities and topological flat bands in magic-angle twisted bilayer graphene. *Nat Mater* **20**, 488–494 (2021).

18. Yu, J. *et al.* Correlated Hofstadter spectrum and flavour phase diagram in magic-angle twisted bilayer graphene. *Nat Phys* **18**, 825–831 (2022).

19. Zondiner, U. *et al.* Cascade of phase transitions and Dirac revivals in magic-angle graphene. *Nature* **582**, 203–208 (2020).

20. Choi, Y. *et al.* Interaction-driven band flattening and correlated phases in twisted bilayer graphene. *Nat Phys* **17**, 1375–1381 (2021).

21. Polshyn, H. *et al.* Large linear-in-temperature resistivity in twisted bilayer graphene. *Nat Phys* **15**, 1011–1016 (2019).

22. Saito, Y. *et al.* Isospin Pomeranchuk effect in twisted bilayer graphene. *Nature* **592**, 220–224 (2021).

23. Jaoui, A. *et al.* Quantum critical behaviour in magic-angle twisted bilayer graphene. *Nat Phys* **18**, 633–638 (2022).

24. Cao, Y. *et al.* Strange Metal in Magic-Angle Graphene with near Planckian Dissipation. *Phys Rev Lett* **124**, 076801 (2020).

25. Kim, H. *et al.* Imaging inter-valley coherent order in magic-angle twisted trilayer graphene. *Nature* **623**, 942–948 (2023).

26. Kwan, Y. H. *et al.* Kekulé Spiral Order at All Nonzero Integer Fillings in Twisted Bilayer Graphene. *Phys Rev X* **11**, (2021).

27. Bultinck, N. *et al.* Ground State and Hidden Symmetry of Magic-Angle Graphene at even Integer Filling. *Phys Rev X* **10**, (2020).

28. Nuckolls, K. P. *et al.* Quantum textures of the many-body wavefunctions in magic-angle graphene. *Nature* **620**, 525–532 (2023).

29. Kumar, A., Xie, M. & Macdonald, A. H. Lattice collective modes from a continuum model of magic-angle twisted bilayer graphene. *Phys Rev B* **104**, (2021).

30. Fischer, A., Klebl, L., Honerkamp, C. & Kennes, D. M. Spin-fluctuation-induced pairing in twisted bilayer graphene. *Phys Rev B* **103**, (2021).

31. Wang, Y., Kang, J. & Fernandes, R. M. Topological and nematic superconductivity mediated by ferro-SU(4) fluctuations in twisted bilayer graphene. *Phys Rev B* **103**, (2021).

32. Morissette, E. *et al.* Dirac revivals drive a resonance response in twisted bilayer graphene. *Nat Phys* **19**, 1156–1162 (2023).

33. Kozii, V., Zaletel, M. P. & Bultinck, N. Spin-triplet superconductivity from intervalley Goldstone modes in magic-angle graphene. *Phys Rev B* **106**, (2022).

34. Dong, Z., Levitov, L. & Chubukov, A. V. Superconductivity near spin and valley orders in graphene multilayers. *Phys Rev B* **108**, 134503 (2023).

35. Kardar, M. *Statistical Physics of Fields*. (Cambridge University Press, 2007). doi:10.1017/CBO9780511815881.

36. Dawson, D. A. Critical dynamics and fluctuations for a mean-field model of cooperative behavior. *J Stat Phys* **31**, 29–85 (1983).

37. Khalaf, E., Bultinck, N., Vishwanath, A. & Zaletel, M. P. Soft modes in magic angle twisted bilayer graphene. *arXiv:2009.14827 [cond-mat.str-el]* (2020).

38. Mehew, J. D. *et al.* Ultrafast Umklapp-assisted electron-phonon cooling in magic-angle twisted bilayer graphene. *Sci Adv* **10**, (2024).

39. He, M. *et al.* Dynamically tunable moiré exciton Rydberg states in a monolayer semiconductor on twisted bilayer graphene. *Nat Mater* (2024) doi:10.1038/s41563-023-01713-y.

40. Hu, Q. *et al.* Observation of Rydberg moiré excitons. *Science (1979)* **380**, 1367–1372 (2023).

Figure Legends

Figure 1. Exciton sensing of isospin orders and dynamics in MATBG. (**a**) Schematics of experimental configuration. An 800nm femtosecond pump pulse creates excitations in MATBG (red), which are then sensed by excitons in an adjacent WSe_2 layer (yellow). (**b**) Equilibrium reflection contrast (RC) of device D1 without the pump excitation. The WSe_2 2s exciton (yellow arrow) shows cascade features at integer fillings of MATBG, while the 1s exciton (blue arrow) shows negligible change. See main text for detailed discussion. (**c**) Transient RC of device D1 at pump probe delay Δt = -3.7, 1, 10 and 136 ps, respectively. The cascade features (arrows) melt upon pump arrival and gradually recover over time. (**d**) Transient RC at ν = 4 before (Δt = -3.7ps) and after (Δt = 1ps) the pump arrival. The 1s exciton remains unaffected, indicating that the 800 nm pump selectively excites MATBG but not WSe_2. On the other hand, 2s exciton shows prominent changes by sensing the excitations in the graphene layers. All measurements are performed at the base temperature of 2.5 K.

Figure 2. Filling dependent dynamics in MATBG. (**a**)(**b**) Pump-induced RC change of device D1 at representative filling factors and temperature of 2.5 K. Prominent slowing-down in relaxation is observed over a broad range of fillings from $\nu = 1.7$ to 2.4 (**a**) and from $\nu = -2.7$ to -1.9 (**b**). (**c**) Pump-induced RC change at the WSe_2 2s exciton resonance across the entire flatband. Vertical dashed lines label even fillings between $\nu = \pm 4$ as guide to the eye. The relaxation lifetime from single exponential fitting shows remarkable increase around $\nu = 2$, -2.3 and ± 4 (**d**, blue curve). On the other hand, only the slowing-down around $\nu = \pm 4$ is prominent in a non-magic angle device D3 (orange curve) that has no apparent cascade features.

Figure 3. Decoupling between the charge and isospin dynamics. (**a**) Temperature dependent relaxation dynamics of device D1 from single exponential fitting. The slowing-down near $v = \pm 4$ does not depend on temperature, indicating a single-particle origin. In contrast, the slowing-down around $v = 2$ and -2.3 largely disappears at 10 K (**b**). (**c**)(**d**) Pump-induced RC change at $v = 2.07$ (**c**) and $v = 3.95$ (**d**) over a larger delay range of 300 ps. Their relaxation dynamics is compared in (**e**). The dynamics at $v = 3.95$ is well-described by a single-component decay with a lifetime of 60 ps (blue symbols and lines); while the dynamics at $v = 2.07$ shows two fully separable timescales, a fast initial decay with lifetime of 10 ps followed by a remarkably long component with lifetime of 300 ps (red symbols and lines). The two fitted curves for $v = 2.07$ are single exponential fitting using experimental data at $\Delta t < 30$ps and $\Delta t > 50$ ps, respectively. (**f**) Similar to (**e**) for the hole side. The dynamics at $v = -3.99$ is captured by a single-component decay with lifetime of 75 ps (blue); while the dynamics at $v = -2.25$ features two separate components with lifetime of 10 ps and 180 ps, respectively (red).

Figure 4. Ultrafast manipulation of the cascade features. (**a**) Delay-dependent evolution of the cascade features on the electron-doping side. The WSe_2 2s exciton energy at each delay is successively shifted up by 1 meV for visual clarity. At equilibrium, the cascade features appear at integer fillings from $\nu = 0$ to 4 (dashed lines). Upon pump excitation, however, the cascade features around ν = 2, 3 and 4 transiently shift to higher fillings and recover over 5 ,10 and 40 ps, respectively, as summarized in (**b**). (**c**) Illustration of a potential mechanism behind the transient shifts of cascade features. Owing to the electron-hole asymmetry, scattering between the remote and the flatbands is efficient for holes (<2ps, left) but slow for electrons (~5 ps at $\nu = 2$, right). As a result, the charge density within the flatband transiently decreases and then recovers over 5 ps. The timescale of such recovery is consistent with the charge dynamics and fully separated from the much longer isospin dynamics.

Methods

Device Fabrication

Graphene, hBN, and WSe_2 flakes used for device fabrication were mechanically exfoliated from bulk crystals onto silicon substrates with a 285 nm silicon oxide layer. The MATBG van der Waals heterostructures were constructed through a standard dry-transfer technique employing a Poly(Bisphenol A carbonate) (PC) film on a polydimethylsiloxane (PDMS) stamp. The fabrication process involved first creating the lower hBN/graphite bottom gate and releasing them onto a 90nm Si/SiO2 substrate. The removal of PC residue on the sample was accomplished by dissolving it in chloroform, followed by rinsing with isopropyl alcohol and vacuum annealing at 375 °C for 12 hours. For the upper part of the heterostructure, we purposely chose hBN with straight edges as the top hBN. Monolayer graphene was cut in half using a Dimension Icon 3100 atomic force microscope (AFM)[41,42]. After picking up the top hBN and monolayer WSe_2, we align the hBN straight edge with the AFM cut on graphene and pick up half of it, twist the silicon substrate with the remaining graphene by 1.06°, pick up the remaining graphene and put down onto the premade bottom part. This stacking sequence was meticulously implemented to minimize the mechanical stretching of the twisted bilayer graphene. Standard electron-beam lithography, dry-etching processes, and vacuum deposition were employed to fabricate electrodes for electrical contacts (~150 nm gold with ~5 nm chromium and ~15nm palladium adhesion layers).

Calibration of carrier density and twist angle

The bottom hBN thickness in the TBG devices was measured by a Dimension Icon 3100 AFM. We computed the geometrical capacitance per unit area between gate and sample through $c_g=\varepsilon_{hBN}\varepsilon_0/d_{hBN}$ where $\varepsilon_{hBN}=3.52$ is the dielectric constant of hBN and d_{hBN} is the bottom hBN thickness. The carrier density in TBG was obtained from $n = c_g V_g/e$, where V_g is the bottom gate voltage and e is the elementary charge. Twist angles of TBG were determined from the spectral features in RC. The WSe_2 2s exciton resonance shows abrupt changes at superlattice filling factors $\nu=\pm4$ (Fig. 1b), allowing the extraction of the corresponding carrier density $n_{\nu=4}$. The twist angle was obtained from $n_{\nu=4} \approx (8\theta^2)/(\sqrt{3}\, a_0^2)$, a_0=0.246nm is the graphene lattice constant.

Reflection contrast measurements

The TBG devices were mounted in a closed-cycle cryostat (Quantum Design, OptiCool) for all optical experiments with a base temperature of 2.5 K. A broadband tungsten lamp was beam-shaped by a single mode fiber and subsequently collimated by a lens. The light was focused onto the sample by an objective (NA=0.45), resulting in a beam diameter of approximately 1µm on sample with a power of approximately 20nW. The reflected light was collected by a liquid-nitrogen-cooled CCD camera coupled with a spectrometer. The reflection contrast was computed as RC=(R'−R)/R, where R' and R represent the reflected light intensity from regions with and without the sample, respectively. Keithley 2400 source meters were employed to apply gate voltages to adjust the charge density.

Pump-probe measurements

All measurements are performed at the temperature of 2.5K and pump fluence of 1.84μJ/cm^2 unless noted otherwise. Femtosecond pulses (1030 nm, 600 kHz, ~200fs) were generated by a regenerative amplifier seeded by a mode-locked oscillator (Light Conversion PHAROS). The femtosecond pulses were split into two parts. One part was used to pump an optical parametric amplifier to generate 800nm excitation laser pulses, used as the pump; and the other part was focused into a sapphire crystal to generate a broadband white light (500 ~ 900 nm) as the probe pulses. The probe light was wavelength selected via a bandpass filter with center wavelength 694nm and 44nm bandwidth. The pump-probe time delay was controlled by a motorized delay stage. To ensure homogeneous spatial profile, both the pump and probe beams were expanded before focusing on the sample and had a diameter of 40 and 10μm on the sample, respectively. The reflected probe light was isolated from the pump light by a 750nm short pass filter and spatially filtered using a 100μm pinhole at an intermediate image plane conjugated with the sample plane. Such a spatial filter isolates responses from a ~2μm diameter region on the sample in the center of the probe beam, thereby ensuring the spatial homogeneity of the probe intensity within the measured region. The filtered probe light was collected by liquid-nitrogen-cooled CCD camera coupled with a spectrometer. Transient RC was computed in the same way as in the equilibrium measurements (Fig. 1 and Fig. 4). To obtain pump-induced RC change (Fig. 2 and Fig. 3), the pump light was modulated by an optical chopper at 20Hz, and the CCD camera was operated in an external trigger mode synchronized with the chopper. This allowed direct isolation of ΔRC from the difference between the spectra with and without the pump.

Pump fluence dependence

Extended Data Fig. 3 shows the relaxation dynamics at ν = 2.07 for three representative pump fluences. Increasing the pump fluence from 0.46μJ/cm^2 to 1.84μJ/cm^2 dramatically changes the initial electronic temperature and the charge cooling rate. The observed ΔRC signal therefore shows sensitive pump fluence dependence at the short timescale of <30ps, which corresponds to the charge dynamics. On the contrary, both the amplitude and dynamics of the slow component >30ps were unaffected by the pump fluence change. The contrasting behaviors between the fast and slow components indicate their distinct origins from the charge and isospin degrees of freedom, respectively, and confirm the complete decoupling between their dynamics.

Fitting of relaxation dynamics

We first fit the relaxation dynamics at all fillings using single exponential decay to avoid the instability of multi-component fitting when the slow component is small. On the other hand, this will considerably underestimate the lifetime of the slow component since the stronger fast component can dominate. The fitted lifetime (Fig. 2d and Fig. 3a) is therefore only for qualitative purposes to identify the range of fillings with the slowing-down behavior. To quantitively extract lifetime of the slow component in this filling range, we fit the experimental data after 50ps with single exponential decay (Fig. 3e and f), where the fast component is expected to be small. For fillings around ν = ±4, the fitted curve using long timescale data also matches well with the experiment at the short timescale <50ps, indicating that the full relaxation dynamics is described by a single component (blue symbols and curves). In contrast, the short and long timescale dynamics around $\nu = \pm 2$ shows distinctive behaviors due to the decoupling between the charge and isospin dynamics and the much longer lifetime of the latter.

Extraction of 2s exciton energy

We extracted the 2s exciton energy at each carrier density from the local maximum in the slope of RC vs. probe energy (Extended Data Fig. 5a). The obtained 2s exciton energy shows a smooth decreasing background with increasing charge density due to stronger screening[39,40]. To highlight the cascade features associated with the isospin physics, we fitted the smooth background using a 3rd-order polynomial (Extended Data Fig. 5b, red curve). The background-subtracted 2s exciton energy shows clear cascade features at integer fillings in equilibrium (Extended Data Fig. 5c). The same background was used for all time delays in pump-probe measurements to ensure that no artifacts were introduced. A peak-finding algorithm was used to determine the filling factors of the cascade features at each time delay (Extended Data Fig. 5c and Fig. 4b).

Comparison between 1s and 2s exciton responses

Fig. 1b shows that the response of WSe_2 2s exciton to doping in the adjacent MATBG is much larger than that of 1s exciton. This observation is consistent with previous reports that the 2s exciton energy in WSe_2 is much more sensitive to dielectric environment than 1s exciton[43,44]. Theoretically, the insensitivity of 1s exciton energy to dielectric screening is a consequence of the cancellation between quasi-particle bandgap shift and exciton binding energy change[43]: a stronger screening will reduce both electron-electron and electron-hole Coulomb interaction, thereby reducing both the quasi-particle bandgap and the exciton binding energy. For 1s exciton, the two effects are comparable, and the quasi-particle bandgap shift is slightly larger. Therefore, stronger screening leads to a slight reduction (redshift) in the 1s exciton energy, which is opposite to the expectation solely from a reduced exciton binding energy. The situation is very different for 2s exciton since its binding energy is much smaller than that of 1s exciton. Therefore, the quasi-particle bandgap shift dominates, giving rise to a much larger overall redshift in the exciton energy. Our observation of prominent 2s exciton redshift with graphene doping and much weaker response from 1s exciton (Fig. 1b) is therefore a natural consequence of dielectric screening from electrons in graphene. Such a difference in behavior between 1s and 2s exciton responses can be used to distinguish between different origins of the observed signal. For example, excitations in the WSe_2 layer, either excitons or free carriers, are expected to lead to larger changes at 1s exciton resonance than at 2s exciton resonance[45–47]. In our pump probe measurements, 2s excitons show prominent changes upon the pump arrival, while the 1s exciton remains largely intact (Fig. 1c). This confirms the origin of the signal from excitations in MATBG instead of in WSe_2.

The strong responses of 2s exciton energy to dielectric environment allow it to sensitively detect isospin orders in MATBG. Isospin orders will reconstruct the Fermi surface of graphene and change its polarizability, thereby affecting the Coulomb screening of 2s exciton in the nearby WSe_2 layer. Therefore, although 2s exciton energy does not couple linearly to spin/valley polarization and or distinguish the sign of order parameter, it is sensitive to the formation of isospin orders and the amplitude of the order parameter. Our observation of cascade features in 2s exciton energy

(Fig. 1b) confirms such sensitivity. Detailed discussions and quantitative simulation of the optical sensing scheme here can be found in Ref.[48].

Effects from the WSe_2 layer

The WSe_2 remains as passive sensor layer throughout the measurements and is not excited by the pump light. As shown in Fig. 1c, the 1s exciton response does not change upon the pump arrival, while the 2s exciton resonance is significantly modified. The much stronger response of 2s exciton than that of 1s indicates that the origin is from change of dielectric environment instead of direct excitations in WSe_2. We have further performed a systematic study of the pump energy dependence (Extended Data Fig. 6, b and c) to unambiguously exclude excitation of WSe_2. Since all pump wavelengths used (800 - 1000nm) are below the optical bandgap of WSe_2 (~740nm), excitation of WSe_2 can only be through in-gap states and/or charge transfer absorption between graphene and WSe_2. Both of these pathways depend sensitively on the pump energy[45,46,49]. On the other hand, the △RC signal we observe is independent of pump wavelength. This indicates that the signal is originating entirely from pump excitations of the MATBG, and WSe_2 remains passive. We also confirm that the probe light does not modify the observed physics. This can in principle be achieved with a sufficiently weak probe. We directly test the probe effects by measuring a probe fluence dependence without the pump light, as shown in Extended Data Fig. 6a. When probe light fluence is too large, the WSe_2 2s resonance is significantly broadened and the cascades features are blurred. On the other hand, at a probe fluence of 46.7nJ/cm^2, which we have used throughout the measurements, the impact of the probe light is minimal.

While the WSe_2 does not generate excitations during the pump probe measurement, its presence can passively affect the phase diagram of the system by e.g. changing the dielectric environment of MATBG and introducing proximity spin-orbit coupling (SOC). However, these effects do not prevent and could actually facilitate the study of correlated physics in MATBG. The effects from adjacent WSe2 layer to flatband graphene are recently under intensive investigation as additional tuning knobs to navigate the correlated phase diagram. In particular, WSe_2/MATBG, the same system as in our work, has been investigated in several studies. Ref.[8] shows that superconductivity is stabilized in small-twist angle MATBG with proximate WSe_2, where superconducting domes emerge at $-3<\nu<-2$ and near $\nu=2$. Ref.[50,51] demonstrates that an adjacent WSe_2 layer can stabilize time-reversal symmetry breaking and Chern insulator states in MATBG at integer fillings of $\nu=2$ and $\nu = 3$. In both cases, the main effects from WSe_2 are proposed to be a proximity SOC introduced into the graphene layers. In our experiments, we expect the adjacent WSe_2 layer to play a similar role as that in Ref.[8,50,51]. Since identical device configurations are used, our results can be combined with the ground state phases obtained in Ref.[8,50,51] to establish a unifying picture of orders and excitations. Compared to MATBG without WSe_2, the phase diagram of WSe_2/MATBG is enriched as the SOC can stabilize both topological states such as Chern insulators[50,51] and correlated states like superconductivity[8]. In particular, recent studies have shown that an adjacent WSe_2 layer seems to generally enhance the superconductivity critical temperature by up to an order of magnitude in flatband graphene systems[8,52]. While complete understanding of the WSe_2 effects warrants further theoretical and experimental studies and is under intensive investigation, the enriched phase diagram of WSe_2/MATBG could facilitate the study of physics in flatband graphene.

Our work based on such a system aligns well with recent efforts in the field and provides new insights into its intriguing phase diagram.

Nature of the $\nu = 0$ state

We conclude that the $\nu = 0$ state in device D1 is a "band insulator" for two reasons. First, the dynamics at $\nu = 0$ does not depend sensitively on temperature between 2.5 to 10K. Second, the dynamics at $\nu = 0$ is largely captured by a single-exponential decay of carrier relaxation (Fig. 2c), while the dynamics around $\nu=\pm2$ is described by two well-separated timescales from the charge and isospin dynamics, respectively (Fig. 3e and f). Overall, the behavior at $\nu = 0$ is qualitatively similar to that at $\nu = \pm4$ but distinctively different from around $\nu=\pm2$. These observations indicate that the $\nu = 0$ state in device D1 is insensitive to temperature and does not host long-lived isospin excitations. The simplest scenario is a band insulator. It could also be a correlated insulator with a large gap and without isospin soft modes. TBG is expected to be gapless at the charge neutral point (CNP) from the Bistritzer-Macdonald model. On the other hand, effects not captured by the model, such as strain[26,53], proximity with WSe_2[50,51], and correlation effects beyond the single particle picture[54,55], could lift the degeneracy and induce a gap at the CNP. In particular, bilayer graphene in proximity with WSe_2 has been consistently observed to show a gap at CNP in both STM and transport[8,50–52,56]. Our observation of gapped CNP is therefore consistent with previous observations and could originate from proximity effects of WSe_2. On the other hand, the size and nature of the gap at CNP in WSe_2/MATBG depends sensitively on details of the device such as twist angle, strain, and alignment with hBN[26,53,57]. Therefore, our observation of a "band insulator" at $\nu = 0$ in device D1 may not represent a general case. Future studies are required to fully understand the nature of CNP states in WSe_2/MATBG, which is beyond the scope of our work.

Origin of the transient cascade feature shifts

The cascade features in MATBG have been attributed to the high temperature parent states of isospin orders[20–22]. Their filling dependence can be phenomenologically understood through the scenario of Stoner instability and analogy to Hund's rule in atoms. Namely, the exchange interactions, which arises from Coulomb interaction between carriers, favor isospin flavors to be either completely filled or empty near integer fillings[15–19,28]. The transient shifts of cascade features therefore can have two possible origins. Either the isospin interactions are altered in a state driven out of equilibrium such that the tendency towards symmetry breaking is enhanced at non-integer fillings; or the effective carrier density relevant to isospin physics is transiently changed. While the former scenario is plausible, the latter can naturally arise from a bottleneck in carrier relaxation between the remote- and flat-bands, as detailed in the main text.

Long-lived isospin modes in a compressible phase

Our main finding is the slow isospin relaxation at $1.7<\nu<2.4$ and $-2.7<\nu<-1.9$ that completely decouples from the much faster carrier cooling. The slowing-down at $-2.7<\nu<-1.9$ is centered notably away from integer fillings, and the relaxation at $\nu = -2.3$ is significantly slower than at $\nu = -2$. These observations are consistent over all three MATBG devices D1, D3 and D4. Extended Data Fig. 7d compares the filling-dependent relaxation time from optical pump-probe measurements and the longitudinal resistance R_{xx} from in-situ four-point transport. The resistance

R_{xx} shows strongly insulating peaks at $\nu=\pm4$ from the gaps between the flat and remote bands. In addition, we also observe resistance peaks exactly at $\nu=\pm2$ and $\nu=\pm3$, corresponding to correlated insulating states[7,8,51,58]. In contrast, the relaxation time behaves quite differently. First, while $\nu=\pm3$ is strongly insulting and more resistive than $\nu=2$, the relaxation time at $\nu=\pm3$ is not significantly enhanced and is much shorter than at $\nu=2$. Second, on the hole doping side the slow isospin dynamics is observed in a broad filling range of $-3<\nu<-2$, and the maximum slowing-down peaks clearly away from the correlated insulators at integer fillings.

Now we discuss the possible origins and implications of these observations. At $\Delta t>30$ps, the system's electronic temperature is already approaching the equilibrium (Fig. 2e and Ref.[38]), and the ΔRC signal becomes independent of the pump driving amplitude (Extended Data Fig. 3). Therefore, the long-timescale dynamics is an intrinsic attribute of the isospin ground states as well as the excitations associated with these states. The observed weak damping and long lifetime of isospin excitations imply that these excitations have lower energy than the particle-hole excitation gap, otherwise they would efficiently decay into the particle-hole continuum. Therefore, a slow isospin relaxation indicates the particle-hole excitation gap is relatively large as compared to the energy of isospin modes. The observed much longer isospin lifetime at $\nu=2$ than at $\nu=1$ and 3 could either be due to a flatter energy landscape in the isospin degree of freedom or a larger gap in the charge degree of freedom at $\nu=2$. Since our transport measurement does not allow quantitative extraction of thermodynamic gap due to the high base temperature of 2.5K, we cannot conclusively distinguish these possibilities.

On the other hand, the most intriguing observation from our experiments is the slow isospin relaxation at $-3<\nu<-2$, i.e., away from integer fillings. This provides direct insights into the properties of both the soft modes and the ground state. The transport measurements (Extended Data Fig. 7d) confirm that this filling range corresponds to a gapless metallic state. Therefore, the long-lived isospin modes are likely also gapless in order to have weak damping. A natural origin of such gapless mode is a broken continuous symmetry, which results in a Goldstone mode as predicted by the Nambu-Goldstone theorem. In MATBG, there are two continuous isospin symmetries --- SU(2) spin-rotation symmetry and a U(1) valley rotation symmetry. Breaking the former symmetry results in spin-polarized order, leading to standard magnon modes. Likewise, breaking U(1) valley rotation symmetry results in intervalley coherence order, which leads to a sliding mode of the Kekulé charge density wave. However, the first possibility can almost certainly be excluded, since the proximity spin-orbit coupling from the adjacent WSe_2 layer breaks the spin rotation symmetry[8,34,59] and gaps out the magnon modes. Therefore, the most likely candidate of the isospin mode that accounts for the abnormal long relaxation at $-3<\nu<-2$ is a gapless Goldstone mode from the U(1) valley rotation symmetry. Here, it should be noted that there are two closely related ground state orders that break the U(1) valley rotation symmetry. One is an IVC state that breaks U(1) valley rotation alone, the other is the incommensurate IKS state, which is essentially an incommensurate version of IVC order, or a charge density wave at a momentum of $\mathbf{K}$-$\mathbf{K}'$+$\boldsymbol{q}$. Such IKS state breaks both valley U(1) and translation T, but preserves a "spiral" translation symmetry T' which simultaneously shifts the spatial coordinates and rotates the U(1) angle[26]. The competition between these two candidate ground states depends on the strain[26]. In general, the IVC state is lower in energy in the absence of strain, whereas the IKS state is favored upon increasing strain. Since they both host Goldstone modes, our measurement cannot resolve which one is the true ground state. Other order types that only break discrete symmetries, such as spin/valley polarized states and states with nematic order, are not likely to account for the observed long relaxation. Weak damping of Goldstone modes in a metallic state can then be intuitively understood from the illustration in Extended Data Fig. 8. The isospin mode primarily couples to S^+ particle-hole excitations that involve an isospin flip. Such S^+ particle-hole continuum, similar to the Stoner continuum in ferromagnets[60], is gapless in a metallic state but must have a finite exchange gap at $q = 0$. As a result, a Goldstone mode with small q is isolated from the isospin particle-hole continuum and remains weakly damped.

It is all but natural to extend our approach to other flatband graphene systems, both moiré and non-moiré. Doing so will help further elucidating the connection between quasiparticle lifetime, collective excitations and correlated orders. Besides the isospin dynamics, the carrier relaxation dynamics and filling-dependent phonon bottleneck determined here provide a direct measure for electron-phonon coupling strength and electron-hole asymmetry in MATBG. The capability of creating transient non-thermal carrier distributions and associated orders opens up the opportunity for ultrafast control of previously studied correlated states and creating new ordered states.

Methods References

41. Li, H. *et al.* Electrode-Free Anodic Oxidation Nanolithography of Low-Dimensional Materials. *Nano Lett* **18**, 8011–8015 (2018).

42. Masubuchi, S., Ono, M., Yoshida, K., Hirakawa, K. & Machida, T. Fabrication of graphene nanoribbon by local anodic oxidation lithography using atomic force microscope. *Appl Phys Lett* **94**, (2009).

43. Hsu, W.-T. *et al.* Dielectric impact on exciton binding energy and quasiparticle bandgap in monolayer WS2 and WSe2. *2d Mater* **6**, 025028 (2019).

44. Xu, Y. *et al.* Creation of moiré bands in a monolayer semiconductor by spatially periodic dielectric screening. *Nat Mater* **20**, 645–649 (2021).

45. Yuan, L. *et al.* Photocarrier generation from interlayer charge-transfer transitions in WS2-graphene heterostructures. *Sci Adv* **4**, (2018).

46. Chen, X., Zheng, S.-W., Wang, X.-P. & Wang, H.-Y. Ultrafast dynamics of spin relaxation in monolayer WSe2 and the WSe2/graphene heterojunction. *Physical Chemistry Chemical Physics* **24**, 16538–16544 (2022).

47. Ezgi Eroglu, Z. *et al.* Filling Exciton Trap-States in Two-Dimensional Tungsten Disulfide (WS2) and Diselenide (WSe2) Monolayers. *Nanomaterials* **11**, 770 (2021).

48. Xie, T. *et al.* Optical Imaging of Flavor Order in Flat Band Graphene. (2024).

49. Jin, C. *et al.* Identification of spin, valley and moiré quasi-angular momentum of interlayer excitons. *Nat Phys* **15**, 1140–1144 (2019).

50. Choi, Y. *et al.* Correlation-driven topological phases in magic-angle twisted bilayer graphene. *Nature* **589**, 536–541 (2021).

51. Lin, J.-X. *et al.* Spin-orbit–driven ferromagnetism at half moiré filling in magic-angle twisted bilayer graphene. *Science (1979)* **375**, 437–441 (2022).

52. Zhang, Y. *et al.* Enhanced superconductivity in spin–orbit proximitized bilayer graphene. *Nature* **613**, 268–273 (2023).

53. Bi, Z., Yuan, N. F. Q. & Fu, L. Designing flat bands by strain. *Phys Rev B* **100**, 035448 (2019).

54. Song, Z.-D. & Bernevig, B. A. Magic-Angle Twisted Bilayer Graphene as a Topological Heavy Fermion Problem. *Phys Rev Lett* **129**, 047601 (2022).

55. Hu, H., Bernevig, B. A. & Tsvelik, A. M. Kondo Lattice Model of Magic-Angle Twisted-Bilayer Graphene: Hund's Rule, Local-Moment Fluctuations, and Low-Energy Effective Theory. *Phys Rev Lett* **131**, 026502 (2023).

56. Zhou, H. *et al.* Isospin magnetism and spin-polarized superconductivity in Bernal bilayer graphene. *Science (1979)* **375**, 774–778 (2022).

57. Uri, A. *et al.* Mapping the twist-angle disorder and Landau levels in magic-angle graphene. *Nature* **581**, 47–52 (2020).

58. Cao, Y. *et al.* Correlated insulator behaviour at half-filling in magic-angle graphene superlattices. *Nature* **556**, 80–84 (2018).

59. Milivojević, M., Gmitra, M., Kurpas, M., Štich, I. & Fabian, J. Proximity-induced spin-orbit coupling in phosphorene on a WSe2 monolayer. *Phys Rev B* **108**, 115311 (2023).

60. Nolting, W. & Ramakanth, A. *Quantum Theory of Magnetism*. (Springer Berlin Heidelberg, Berlin, Heidelberg, 2009). doi:10.1007/978-3-540-85416-6.

61. Xie, T. Long lived isospin excitation in magic angle twisted bilayer graphene. (2024). Available at: osf.io/8kqh3.

Acknowledgements

We acknowledge discussions with Andrea Young and Leon Balents. C.J. acknowledges support from Air Force Office of Scientific Research under award FA9550-23-1-0117. The sample fabrication is supported by National Science Foundation (NSF) through a CAREER award DMR-2337606. T.X. acknowledges the support from the National Science Foundation Graduate Research Fellowship under Grant No.2139319. L.L. acknowledges the support from the Science and Technology Center for Integrated Quantum Materials, National Science Foundation Grant No. DMR1231319. S.T acknowledges primary support from DOE-SC0020653 (materials synthesis), DMR 2111812, DMR 2206987 and CMMI 2129412 (manufacturing). S.T acknowledges support from Lawrence Semiconductor Labs. K.W. and T.T. acknowledge support from the JSPS KAKENHI (Grant Numbers 20H00354 and 23H02052) and World Premier International Research Center Initiative (WPI), MEXT, Japan.

Contribution

C.J. conceived and supervised the project. S.X., Z.C., and T.X. fabricated the device. T.X. performed the measurements and analyzed the data. Z.D. and L.L. contributed to the theoretical interpretation. Y.O., M.E., and S.T. grew the WSe_2 crystals. K.W. and T.T. grew the hBN crystals. C.J. wrote the manuscript with the input from all the authors.

Competing interests

The authors declare no competing interests.

Additional Information

Correspondence and requests for materials should be addressed to Chenhao Jin

Data availability statement

All data in the main text and extended figures, as well as the code for data analysis, are available from Open Science Framework[61].

Extended Data Figure Legends

Extended Data Figure 1. Dynamics in MATBG device D2 (1.06° twisted). (**a**) Equilibrium RC. (**b**) Pump-induced RC change (ΔRC) at representative filling factors and temperature of 2.5 K. Prominent slowing-down in relaxation is observed over a broad range of fillings near $\nu = 2$. (**c**) ΔRC at the WSe_2 2s exciton resonance across the entire flatband and (**d**) the filling-dependent lifetime from single exponential fitting. The slowing-down is maximized around $\nu = 2.1$ and -2.3, consistent with the observation in device D1. Vertical dashed lines label even fillings between $\nu = \pm 4$ as guide to the eye. (**e**)(**f**) ΔRC at $\nu = 2.04$ (**e**) and $\nu = 3.99$ (**f**) over a larger delay range of 300 ps. Their relaxation dynamics are compared in (**g**). The dynamics at $\nu = 3.99$ is well-described by a single-component decay with a lifetime of 60 ps (blue symbols and lines); while the dynamics at $\nu = 2.04$ shows two fully separable timescales with lifetime of 15 ps and 315 ps, respectively.

Extended Data Figure 2. Dynamics in non-magic-angle TBG device D3 (1.14° twisted). (**a**) Equilibrium RC. (**b**) Pump-induced RC change at temperature of 2.5 K and representative fillings. No apparent slowing-down is observed near $\nu = 2$.

Extended Data Figure 3. Pump fluence dependence. (**a**) Pump-induced RC change for device D1 at $\nu = 2.07$ under three representative pump fluences. (**b**) Comparison between the relaxation dynamics. The fast component shows sensitive pump fluence dependence due to different initial electronic temperature, as expected from the charge dynamics. In contrast, the slow component is insensitive to the pump fluence, indicating a complete decoupling between the isospin and charge dynamics.

Extended Data Figure 4. Temperature dependence of Equilibrium RC. The cascade features become weaker and broader at higher temperatures but do not show apparent shift in fillings.

Extended Data Figure 5. Extraction of 2s exciton energy. (**a**) Representative RC of device D1 with the extracted 2s exciton energy overlaid on top (green line). (**b**) Filling-dependent 2s exciton energy (blue) and a fitted 3^{rd}-order polynomial accounting for the smooth background redshift (orange). (**c**) The background-subtracted 2s exciton energy (blue line) shows clear peaks from the cascade features, whose locations are obtained by a peak finding algorithm (orange arrows).

Extended Data Figure 6. Probe fluence and pump wavelength dependence. (**a**) RC of device D4 without pump and under representative probe fluences. The cascade features are blurred at higher probe fluence. On the other hand, the impacts from the probe light are negligible at probe fluence of 46.7nJ/cm^2, which we have used throughout our measurements. (**b**)(**c**) Pump-induced RC change at ν = -2.36 (**b**) and ν = 2.05 (**c**) with pump wavelengths of 800, 900, and 1000nm and pump fluence of 1.84μJ/cm^2. The signal remains largely unchanged across these pump wavelengths, confirming that the pump is selectively exciting MATBG and the WSe_2 layer remains a passive sensor.

Extended Data Figure 7. Dynamics in MATBG device D4 (0.95° twisted). (**a**) Equilibrium RC. (**b**) Pump-induced RC change of device D4 at representative filling factors and temperature of 2.5 K. Prominent slowing-down in relaxation is observed over a broad range of fillings between ν = -3 and -2. (**c**) ΔRC at the WSe_2 2s exciton resonance across the entire flatband. (**d**) Filling-dependent lifetime from single exponential fitting (blue curve) and longitudinal resistance R_{xx} from in-situ four-point transport measurement (orange curve). The slowing-down on the hole-doping side is maximized around ν = -2.4, a gapless metallic state, consistent with the observation in device D1 and D3. (**e**) Temperature dependence of longitudinal resistance R_{xx}.

Extended Data Figure 8. Illustration of weakly damped isospin Goldstone mode in a metallic state. The energy-momentum dispersion of the isospin particle-hole continuum can have a finite gap at q = 0, allowing the Goldstone mode to remain weakly damped.

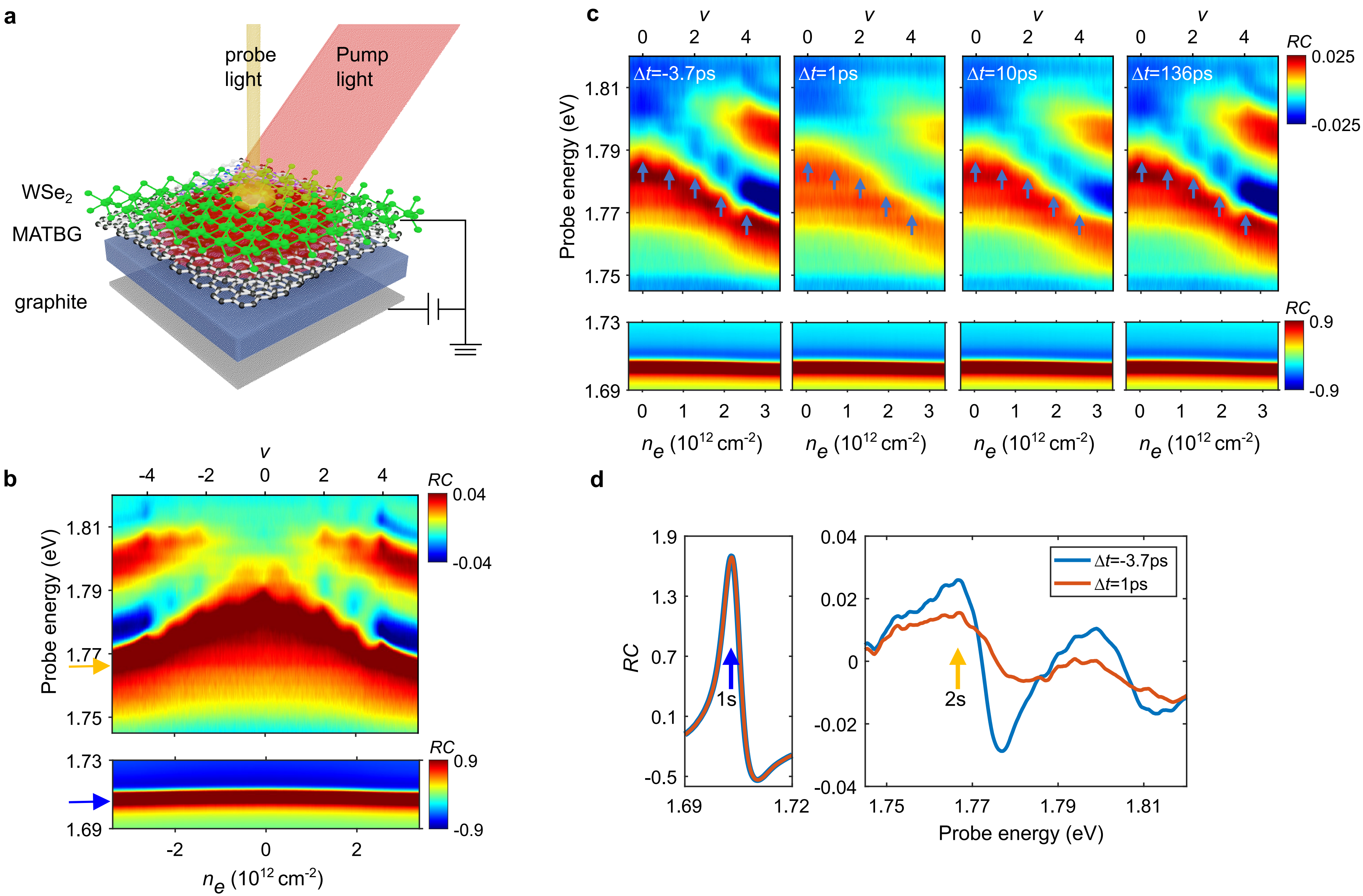

a
probe light
Pump light
WSe2
MATBG
graphite
b
v
Probe energy (eV)
RC
0.04
-0.04
0.9
-0.9
n_e (10^{12} cm^{-2})
c
Δt=-3.7ps
Δt=1ps
Δt=10ps
Δt=136ps
RC
0.025
-0.025
d
1s
2s
Δt=-3.7ps
Δt=1ps
Probe energy (eV)

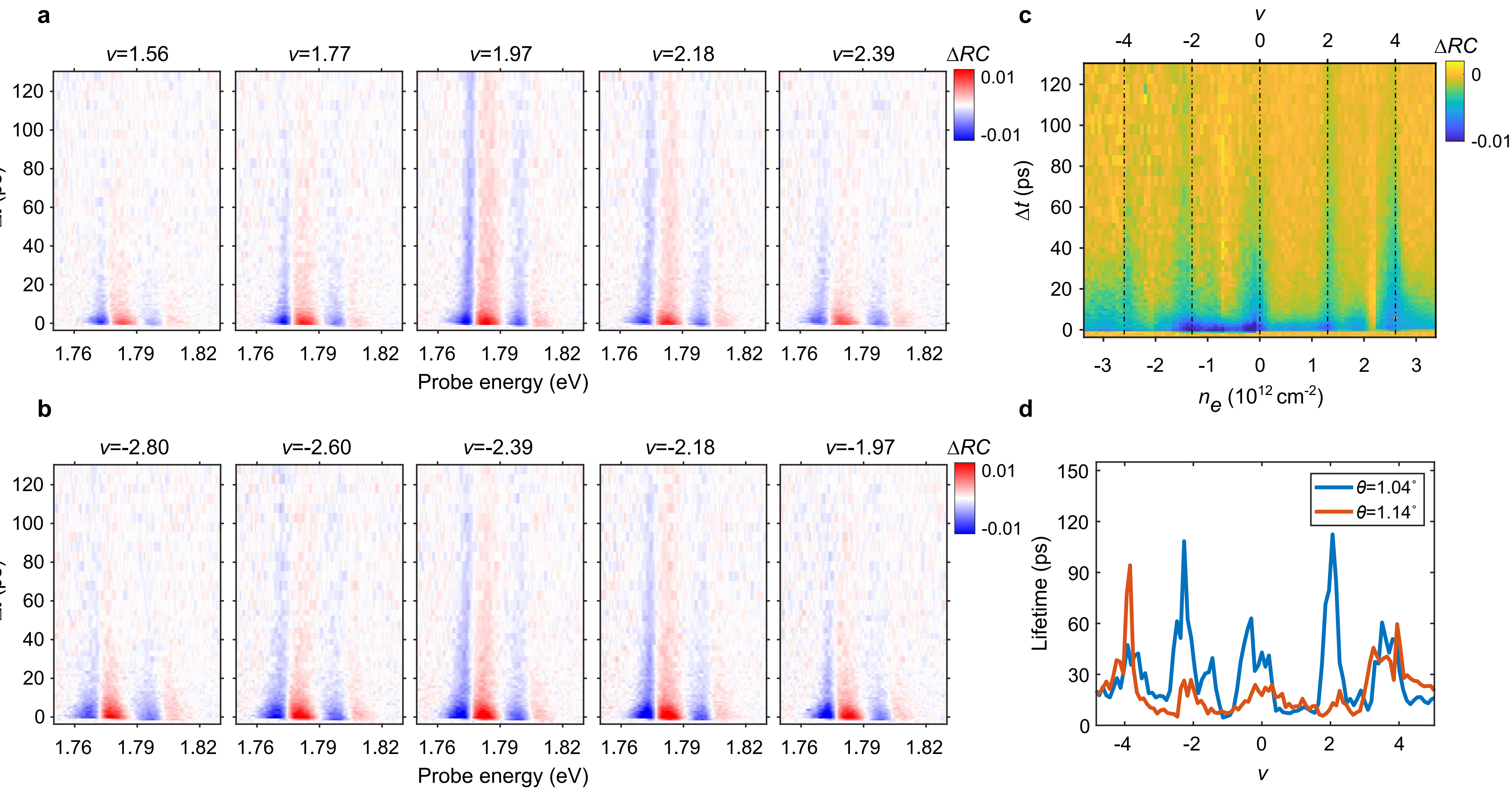

a
v=1.56
v=1.77
v=1.97
v=2.18
v=2.39
ΔRC
0.01
-0.01
Δt (ps)
Probe energy (eV)
b
v=-2.80
v=-2.60
v=-2.39
v=-2.18
v=-1.97
c
v
n_e (10^{12} cm^{-2})
d
θ=1.04°
θ=1.14°
Lifetime (ps)

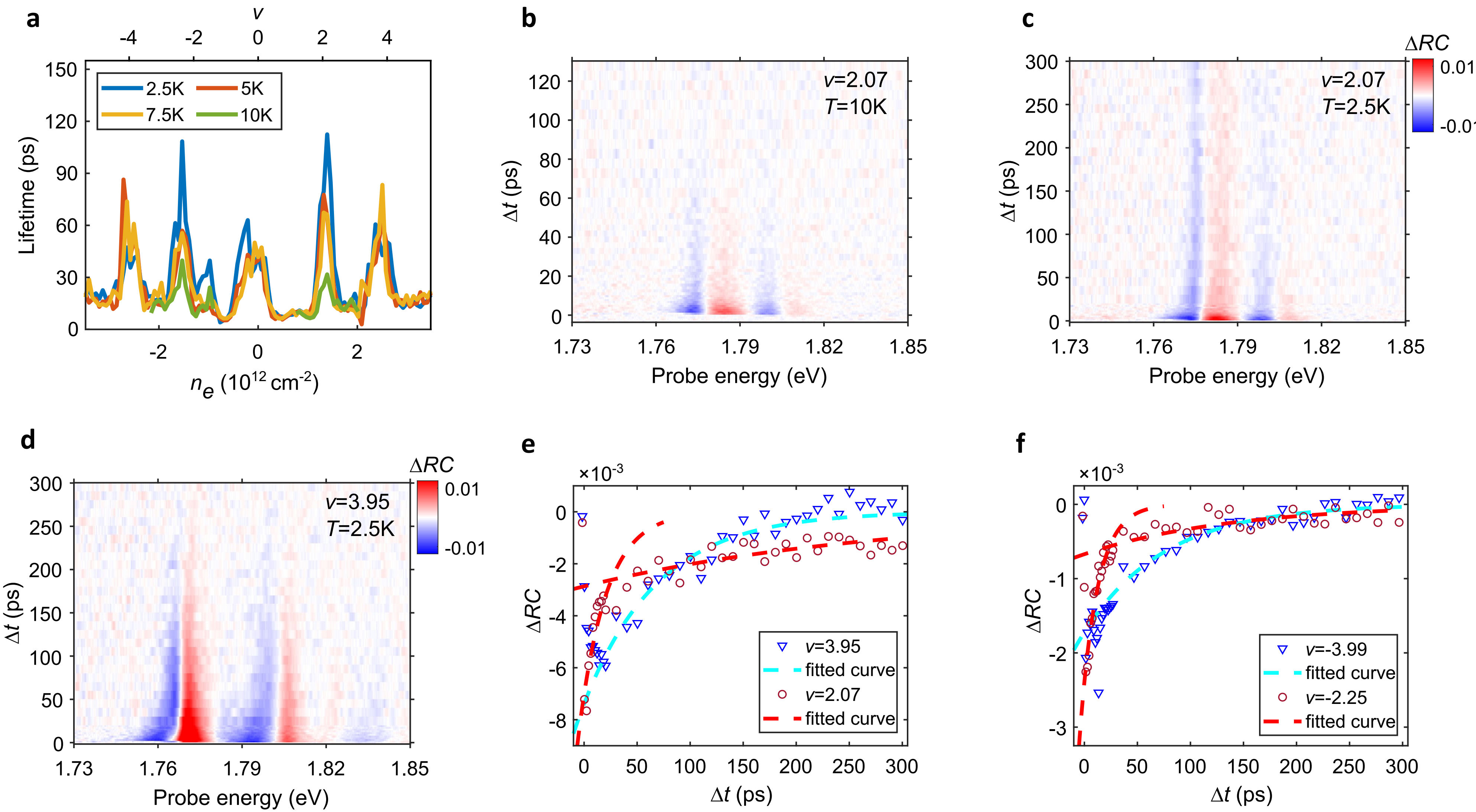
a
b
c
d
e
f
v
Lifetime (ps)
n_e (10^{12} cm^{-2})
2.5K
5K
7.5K
10K
Δt (ps)
Probe energy (eV)
v=2.07
T=10K
T=2.5K
v=3.95
ΔRC
0.01
-0.01
×10^{-3}
v=3.95
fitted curve
v=2.07
v=-3.99
v=-2.25

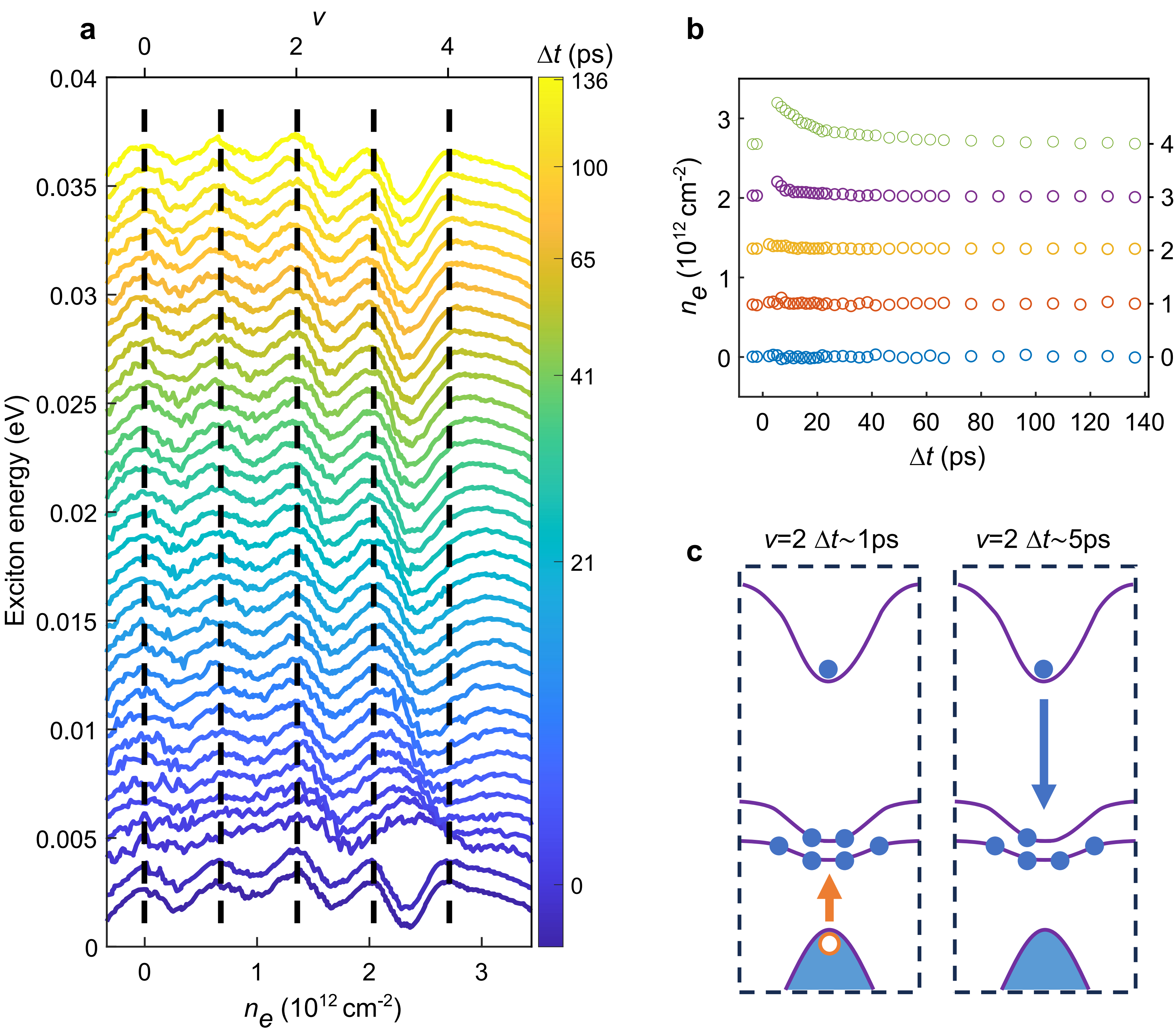

a
b
c
v
Δt (ps)
Exciton energy (eV)
n_e (10^{12} cm^{-2})
Δt (ps)
v=2 Δt~1ps
v=2 Δt~5ps